Optics & Laser Technology 152 (2022) 108151

Contents lists available at ScienceDirect

Optics and Laser Technology

journal homepage: www.elsevier.com/locate/optlastec

Dynamic evolution of keyhole during multi-pulse drilling with a millisecond laser on 304 stainless steel

Yue Zhang [a,c], Xiuli He [a,c,*], Gang Yu [a,b,c,*], Shaoxia Li [a,c], Chongxi Tian [a,c], Weijian Ning [a], Yanmei Zhang [a,c]

[a] Institute of Mechanics, Chinese Academy of Sciences, Beijing 100190, China
[b] Center of Materials Science and Optoelectronics Engineering, University of Chinese Academy of Sciences, Beijing 100049, China
[c] School of Engineering Science, University of Chinese Academy of Sciences, Beijing 100049, China

ARTICLE INFO

Keywords:
Laser drilling
Keyhole evolution
Driving forces
Flow pattern
Numerical simulation

ABSTRACT

The efficiency of millisecond laser drilling is high due to the molten material ejection, and is applied in many industries like aerospace, automobile and electronics. However, there may be some defects such as hole blockage, low machining accuracy and low repeatability, especially for the process of multi-pulse drilling. The melt flow remaining inside keyhole due to inefficient ejection, is responsible for the formation of those defects. Hence, it is necessary to investigate the dynamic behavior of melt flow during multi-pulse drilling. In this paper, the dynamic evolution of keyhole is investigated combining in-situ observation and numerical simulation methods. According to the ejection efficiency, the multi-pulse drilling process can be divided into three periods, namely rapid drilling period, linear drilling period, and moderate drilling period. The melt flow behaves differently in each period. In rapid drilling period, a conical keyhole is formed in the end. The melt flow behavior is affected dominantly by the recoil pressure when the laser is on and by the surface tension when the laser is off. In linear drilling period, the blocked keyhole occurs occasionally. The melt flow behavior is affected by gravity and recoil pressure when the laser is on and by the surface tension and recoil pressure when the laser is off. In moderate drilling period, the keyhole profile is wavy. The melt flow behavior is affected by surface tension and recoil pressure dominantly during the whole period. The melt flow transition and its influence factors are investigated in this paper, which is helpful for understanding the physical processes during the multi-pulse laser irradiation process.

1. Introduction

Laser drilling is a popular non-traditional machining process for production of precise micro-holes (cooling holes and fuel nozzles, et. al.) of vital components (turbine blade and engines, et. al.), by virtue of high accuracy, high flexibility, and high efficiency. In the process of laser drilling, the efficiency and quality of drilling are affected by the physical properties of metal material and the process parameters of laser drilling. When the pulse duration is short or ultra-short (ns, ps, fs), the peak power of laser is extremely high ($\geq 10^{13}$ W/cm^2) and the material vaporized directly. Hence, the hole is drilled with high quality and low efficiency. On the contrary, when the pulse duration is long (μs, ms), the material melts and is then ejected due to recoil pressure caused by vaporization. As a result, the material removal rate is high. For example, Perrie et al. [1] performed a laser drilling on alumina ceramic with Clark-CPA 2010 femtosecond laser and the material removal rate was about 0.054 mm^3/min. However, Voisey et al. [2] drilled a hole with Nd:YAG millisecond laser and the material removal rate was about 27.4 mm^3/min.

In application, in order to increase cooling effectiveness, the aspect ratio of cooling holes or fuel nozzles is usually high. Kampe et al. [3] performed a numerical simulation for predicting the flow structure of outflow from cylindrical holes, and proved that the outflow velocity profile was uniform when the aspect ratio of cooling holes was high. Besides, Liu et al. [4] indicated that the aspect ratio of cooling holes in aero-engine was up to 10, and the thickness of base material was up to 4 mm. Zhai et al. [5] also pointed out that there were about 30,000 holes in a turbine blade. Hence, high aspect ratio, thick base material and quantity production are frequent processing requirements for laser drilling in industrial application. In this instance, multi-pulse drilling

* Corresponding authors at: Institute of Mechanics, Chinese Academy of Sciences, Beijing 100190, China.
E-mail addresses: xlhe@imech.ac.cn (X. He), gyu@imech.ac.cn (G. Yu).

https://doi.org/10.1016/j.optlastec.2022.108151
Received 6 December 2021; Received in revised form 8 March 2022; Accepted 5 April 2022
Available online 12 April 2022

with a millisecond laser, during which drilling efficiency is high, is more suitable for industrial applications.

During long-pulse laser drilling process, the laser power density is usually high. For instance, Chen et al. [6] observed the single-pulse laser drilling process with in situ observation system. They pointed out that the irradiated material melted and was mostly ejected due to the high laser power density in the initial stage. Duan et al. [7] performed a drilling experiment with temporally modulated laser pulses on Inconel 718 sheet. Under the condition of the optimum drilling parameters, the thickness of the melt layer was about 2.5 μm. In this case, the melt flow could be considered as one-dimensional laminar flow. Based on this assumption, Ki et al. [8] developed a numerical model with capturing the vapor/liquid interface and coupling the interaction physics such as thermo-capillary force, recoil pressure and multiple reflection. The predicted keyhole profile and material removal rate were consistent with the experimental results. Besides, when the laser power density is high enough, the drilling process is affected by the heat conduction effect dominantly rather than the flow effect. In this condition, the melt flow could even be neglected for simplifying the calculation.

However, these assumptions are not satisfied all the time due to the Gaussian distribution of laser beam. During the process of multi-pulse drilling (defocus amount is 0), the keyhole depth increases with the increase of pulse number. Ho et al. [9] monitored the laser induced plasma emission with a coaxial photodiode, and found that the efficiency for melt ejection and drilling decreased simultaneously when reaching a certain depth. Arrizubieta et al. [10] investigated the internal characterization of drilled hole by 3D reconstruction technology for hole geometry, and pointed out that the unejected material flowed back and remained inside keyhole during the laser-off period due to the inefficient ejection. Alavi et al. [11] combined the numerical simulation method and in situ observation method to investigated evolution of quality features during laser drilling, and found that the molten material may coalesce locally inside keyhole and caused a keyhole blockage when the ejection was inefficient. Sharma et al. [12] investigated the induced mechanism for keyhole blockage through the use of a hydrodynamics numerical model. They indicated that a downward flow induced by gravity collided with an upward flow induced by recoil pressure, which was the main reason that the blockage occurred. Walther et al. [13] proposed a method to improve the drilling reproducibility and investigated the related mechanism. They pointed out that the blockage remelted or reopened randomly under the irradiation of the subsequent laser pulses, hence the accuracy of repetitive machining was poor. It can be seen from the above, the defects such as hole blockage, low machining accuracy and low repeatability are associated with the behavior of fluid dynamic. Hence, the melt flow cannot be neglected or simplified as a one-dimensional laminar flow during multi-pulse drilling.

In conclusion, some progress has been made on the dynamic evolution of drilled keyhole. During single pulse drilling, the melt flow usually be neglected or simplified as a one-dimensional laminar flow for the simulation. During multi-pulse drilling, melt pool behavior is more complicated due to longer irradiation time and higher aspect ratio. Although the evolution of hole geometry and induced mechanism of keyhole blockage in multi-pulse drilling have been investigated, the transition of flow pattern and effect of driving forces still need be further systematically studied. More importantly, due to the Gaussian distribution of laser beam, the laser power density at keyhole profile is dynamically changing. As a result, the melt temperature changes spatially. Besides, the melt temperature increases when the laser is on and decreases when the laser is off. Hence, the melt temperature changes temporally. The driving forces such as recoil pressure, surface tension, and gravity are the function of temperature, which leads to a variant force system and dynamically changing flow. In such a Time-Varying System (TVS), dynamic evolution of keyhole, the transition mechanism of melt fluid, the effect of each driving force on dynamic evolution and transition mechanism, under varying laser power density, have hardly ever been investigated.

Therefore, in this paper, in order to investigate the fluid dynamics of melt, a three-dimensional numerical model was developed. In the model, through the use of a volume of fluid (VOF) method, the evolving vapor/liquid interface was captured. Then the thermal, velocity and pressure boundary conditions at vapor/liquid interface could be changed adaptively. In the end, the change of driving forces over time and the impacts of that on flow behavior could be studied. Besides, for the purpose of evaluating the drilling quality, an observation system with high speed camera was established. Ultimately, by combining the optical observation and numerical simulation, the dynamic behavior of melt flow during multi-pulse drilling was investigated.

2. Numerical simulation

2.1. Assumptions

In order to simplify the modeling and improve the computing efficiency, the numerical model was developed in the view of following assumptions:

1. The laser energy input was treated as a Gaussian surface heat source. In addition, the influence of plasma shielding, inverse bremsstrahlung absorption, multiple Fresnel absorption, and divergence of the laser beam were ignored.
2. Metallic vapor was considered as an ideal gas, and the dynamics of vapor plume and the condensation of vapor were neglected for simplicity.
3. The melt flow of the molten material was considered as incompressible Newtonian laminar flow.
4. The material properties differed so tremendously between gas and liquid, hence the values were smoothed out for numerical purpose.
5. The mushy region between solidus line and liquidus line was an isotropic porous medium.

2.2. Governing equations

The governing equations for mass, momentum and energy conservation are expressed in Cartesian coordinates as follows:

$$\frac{\partial \rho}{\partial t}+\frac{\partial(\rho u_i)}{\partial x_i}=0 \tag{1}$$

$$\frac{\partial(\rho u_i)}{\partial t}+\frac{\partial(\rho u_i u_j)}{\partial x_i}=\frac{\partial}{\partial x_i}\left(\mu\frac{\partial u_j}{\partial x_i}\right)+S_{u_i} \tag{2}$$

$$\frac{\partial(\rho C_p T)}{\partial t}+\frac{\partial(\rho u_i C_p T)}{\partial x_i}=\frac{\partial}{\partial x_i}\left(k\frac{\partial T}{\partial x_i}\right)+S_E \tag{3}$$

where ρ represents the density, u_i represents the velocity component in the x_i direction, t represents the time, μ represents the dynamic viscosity, C_p represents the specific heat capacity, T represents the temperature, k represents the thermal conductivity, S_{u_i} and S_E represent the energy source term and momentum source term, namely, and are expressed as follows:

Energy source term:

$$S_E=-\frac{\partial \Delta H_m}{\partial t}-\frac{\partial(\rho u_i \Delta H_m)}{\partial x_i}+q_{lv}\left(\frac{2\rho C_p}{\rho_l C_{pl}+\rho_g C_{pg}}\right) \tag{4}$$

Momentum source term:

$$S_{u_i}=-\frac{\partial p}{\partial x_i}+\frac{\partial}{\partial x_j}\left(\mu\frac{\partial u_j}{\partial x_i}\right)-F_{Darcy}+F_{\text{Body}} \tag{5}$$

where ΔH_m represents the latent enthalpy content of the fusion, q_{lv} represents the heat flux at vapor/liquid interface, p represents the pressure, F_{Darcy} represents Darcy damping force driven from Carman-

Kozeny equation, which can be used to calculate the frictional dissipation in the mushy region[14], F_{Body} represents the buoyancy force induced by temperature according to Boussinesq assumption. The Darcy force and body force are defined as follows:

$$F_{Darcy} = K_0 \frac{(1-f_l)^2}{f_l^3 + B} u_i \tag{6}$$

$$F_{Body} = \rho g \beta (T - T_0) \tag{7}$$

where K_0 represents the mushy zone morphology, B is a small number used to avoid the division by zero, f_l represents the liquid fraction, g denotes the acceleration of gravity, and T_0 denotes the atmospheric temperature. The liquid fraction is described as:

$$f_l = \begin{cases} 1 & T > T_l \\ \dfrac{T - T_S}{T_l - T_S} & T_S \le T \le T_l \\ 0 & T < T_S \end{cases} \tag{8}$$

where T_S represents the solidus temperature and T_l represents the liquidus temperature.

2.3. Initial and boundary conditions

The temperature is set as atmospheric temperature T_0 and the velocities are set as 0 for the entire computational domain at initial time. Only heat convection and radiation are considered at the boundary surfaces, hence the thermal and velocity boundary conditions for the boundary surfaces are listed as follows:

$$k\frac{\partial T}{\partial n} = -h_c(T - T_0) - \sigma_b \varepsilon \left(T^4 - T_0^4\right) \tag{9}$$

$$u_i = 0 \tag{10}$$

where n is the normal direction of the boundary surfaces, h_c represents the convective heat transfer coefficient, σ_b denotes the Stefan-Boltzmann constant, and ε is the emissivity.

2.4. Heat source model

As shown in Eq. (4), the thermal boundary condition at vapor/liquid interface is treated as source term. And the heat flux at vapor/liquid interface in Eq. (4) is formulated as follow:

$$q_{lv} = \frac{2QA_{Fre}}{\pi r_b^2} \exp\left(\frac{-2\left((x-x_0)^2 + (y-y_0)^2\right)}{r_b(z)^2}\right) - h_c(T - T_0) - \sigma_b \varepsilon \left(T^4 - T_0^4\right) - \rho_l L_v F_{vap} \tag{11}$$

where Q is the laser power, A_{Fre} is the Fresnel absorption coefficient, $r_b(z)$ is the laser beam radius, x_0 and y_0 are the central position of laser focus. L_v is the latent heat of vaporization, F_{vap} is the speed function of the vapor/liquid interface due to vaporization and formulated as follow:

$$F_{vap} = \frac{\dot{m}_{vap}}{\rho_l} \tag{12}$$

where m_{vap} is the net mass loss due to vaporization and formulated as [15]:

$$\dot{m}_{vap} = P_{sat}(T)\left(\frac{m_{mol}}{2\pi R_v T}\right) \tag{13}$$

where R_v is gas constant, m_{mol} is the molar mass of the evaporated gas, $P_{sat}(T)$ is the saturation pressure at temperature T, which is calculated through Clausius-Clapeyron relation [16]:

$$P_{sat}(T) = P_{Atm} \exp\left(\frac{-L_v m_{mol}}{R_v}\left(\frac{1}{T} - \frac{1}{T_v}\right)\right) \tag{14}$$

where P_{Atm} is the ambient pressure, T_v represents the boiling point of the metal material.

Due to Gaussian-like distribution assumption, the radius at position z along with the axis of laser beam is described as:

$$r_b(z) = r_0 \sqrt{1 + \left(\frac{z - z_0}{Z_R}\right)^2} \tag{15}$$

where r_0 is the laser beam radius at focus position, z_0 represents the defocus position which is 0 in this study, Z_R represents the Rayleigh length.

The laser is circularly polarized and infrared, and the molten surface is fairly smooth, thus the Fresnel absorption coefficient is formulated and simplified as follow according to Hagen–Rubens relation [17]:

$$A_{Fre} = 1 - \frac{1}{2}\left(\frac{1 + (1 - \varepsilon_F \cos\theta)^2}{1 + (1 + \varepsilon_F \cos\theta)^2} + \frac{\varepsilon_F^2 - 2\varepsilon_F \cos\theta + 2\cos^2\theta}{\varepsilon_F^2 + 2\varepsilon_F \cos\theta + 2\cos^2\theta}\right) \tag{16}$$

where θ is the angle of incidence, ε_F is a coefficient related to laser types and material. The value of ε_F is 0.25 in the simulation [18].

2.5. Driving forces at the vapor/liquid interface

The hydromechanics boundary condition at the vapor/liquid interface is formulated as follow:

$$p_{vl} = p_{re} + \sigma n^* \kappa - \nabla_S T \frac{d\sigma}{dT} \tag{17}$$

where p_{vl} is the pressure at the vapor/liquid interface, σ is the surface tension, n^* is the normal vector, κ is the curvature of the vapor/liquid interface, and P_{re} is the recoil pressure and defined as [19]:

$$p_{re} \cong 0.54 P_{sat}(T) \tag{18}$$

A simplified surface tension model is adopted and represented mathematically as follows:

$$\sigma = \sigma_m^0 + \frac{d\sigma}{dT}(\mathrm{T} - T_m) \tag{19}$$

where σ_m^0 represents the surface tension at melting point of metal material T_m.

2.6. Numerical solutions

In order to reduce the time consumed, the computational domain is set as 1 mm × 1 mm × 4 mm as shown in Fig. 1. The upper part is air, and the lower part is 304 stainless steel. The focus position for the laser beam is at the center of top surface for the metal, and a keyhole is formed inside metal domain during the drilling process. The grid size is 0.04 mm × 0.04 mm × 0.06 mm and the time step is 10^{-6}s. The laser parameters for multi-pulse drilling are selected as follows: pulse width of 0.6 ms, repetition rate of 100 Hz, laser power of 1800 W, defocus distance of 0, pulse number of 10, and focal spot diameter of 0.22 mm. Because the pulse width is 0.6 ms and repetition rate is 100 Hz, the heating time is 0.6 ms and cooling time is 9.4 ms within a pulse cycle. Owing to enough cooling time, the molten material inside keyhole has already solidified before the subsequent pulse. Under the chosen computing strategy, the multi-pulse drilling process is computed by a computing platform with 12 × 2.5 GHz CPU, and the total computing time is about 1 h. The thermo-physical parameters for the 304 stainless steel is listed at Table 1.

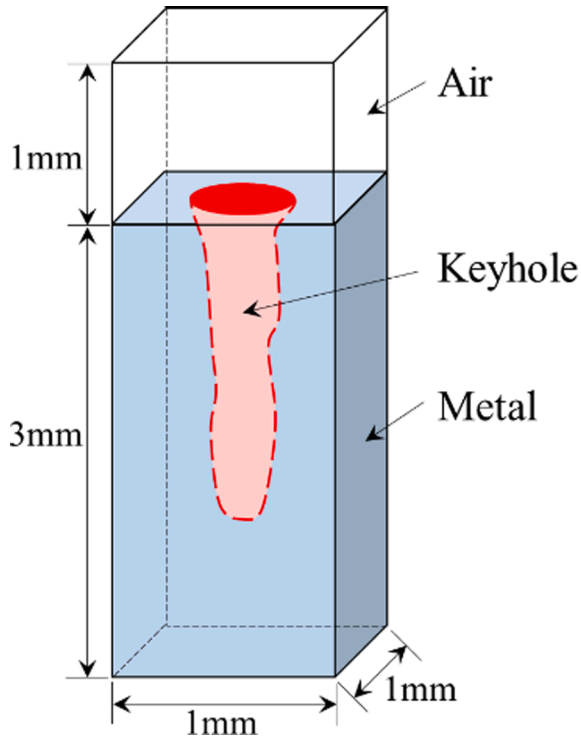

Fig. 1. Schematic diagram of the computational domain.

Table 1
Thermo-physical parameters for the 304 stainless steel [20].

Properties	Value
Solid density ($kg \cdot m^{-3}$)	7200
Liquid density ($kg \cdot m^{-3}$)	6900
Emissivity	0.4
Viscosity ($kg \cdot m^{-1} \cdot s^{-1}$)	0.1
Solidus temperature (K)	1697
Melting temperature (K)	1727
Boiling temperature (K)	3200
Latent heat of vaporization ($J \cdot kg^{-1}$)	6.34×10^{6}
Solid specific heat ($J \cdot kg^{-1} \cdot K^{-1}$)	711.8
Liquid specific heat ($J \cdot kg^{-1} \cdot K^{-1}$)	837.4
Thermal conductivity ($J \cdot m^{-1} \cdot s^{-1} \cdot K^{-1}$)	19.26
Convective heat transfer coefficient ($W \cdot m^{-2} \cdot K^{-1}$)	40
Temperature coefficient of surface tension ($N \cdot m^{-1} \cdot K^{-1}$)	-0.43×10^{-3}
Surface tension ($N \cdot m^{-1}$)	1.96×10^{-5}
Coefficient of thermal expansion	1.872

3. Experimental procedure

In order to observe the dynamic behavior of fluid during multi-pulse drilling with a millisecond laser on 304 stainless steel, an in-situ observation system was established as shown in Fig. 2. Due to the opaque metal material, the keyhole inside metal was invisible and a "sandwich" structure was used. Two JGS1 quartz glasses were chosen due to the characteristic of transparency and high temperature resistance, and the size was set as $100 \times 30 \times 10$ mm^3. A thin plate of 304 stainless steel was sandwiched between the two quartz glasses, and the size was set as $100 \times 30 \times 0.2$ mm^3. The focus diameter of the laser beam was 0.22 mm, which was a little larger than the thickness of the metal plate. In order to make the observed image clearer, the laser induced intense light was attenuated by a neutral filter with 3% transmittance. The experimental work was carried out with a Nd:YAG pulsed laser machine and an i-Speed 221 high speed camera. The photographic parameters were selected as follows: resolution of 192×484 pixels, recording rate of 100 00f/s, and the shutter speed of 1/10000 s. For protecting the focal lens and highlight the influence of recoil pressure, the pressure of assist gas was low, which was about 0.1 MPa.

4. Results and discussion

4.1. Evolution of the keyhole profile

The evolution of the keyhole profile during multi-pulse drilling process was investigated by in-situ observation system as shown in Fig. 3. The melt ejection, molten material inside keyhole, and the keyhole profile could be observed. The observed images in Fig. 3 were captured at the end of heating time and beginning of cooling time in a pulse cycle. At this time, the strong light was mainly from the molten material and the weak light was from the other materials such as plasma or heated wall. Due to the pixel gray difference among the substrate material, molten material, and plasma, an edge detection algorithm of Canny [21] was used in order to observe the keyhole profile and molten material more clearly.

The boundaries of keyhole and molten material were identified as shown in Fig. 4. According to the material removal rate, the keyhole evolution could be divided into three periods: rapid drilling period (AB), linear drilling period (BC), and moderate drilling period (CD). During the rapid drilling period, the keyhole depth increased rapidly as the number of laser pulse increased. There was much melt ejection near the entrance. Inside keyhole, some molten material remained and the liquid layer was thin, and the keyhole was conical. During the linear drilling period, the depth of keyhole varied linearly as the number of laser pulse increased. The melt ejection near the entrance gradually vanished. Inside keyhole, there was some molten material remaining as indicated with white dotted circles in Fig. 4. The molten material solidified at the end of pulse cycle and keyhole blockage occurred. During the moderate

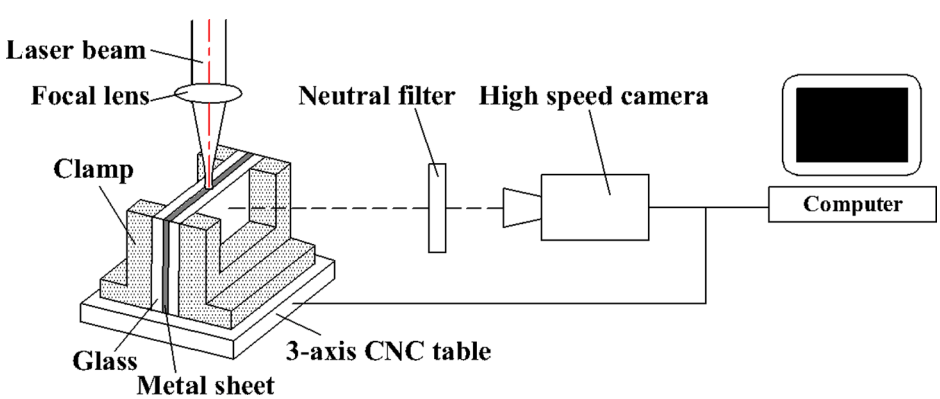

Fig. 2. Schematic diagram of the in-situ observation system.

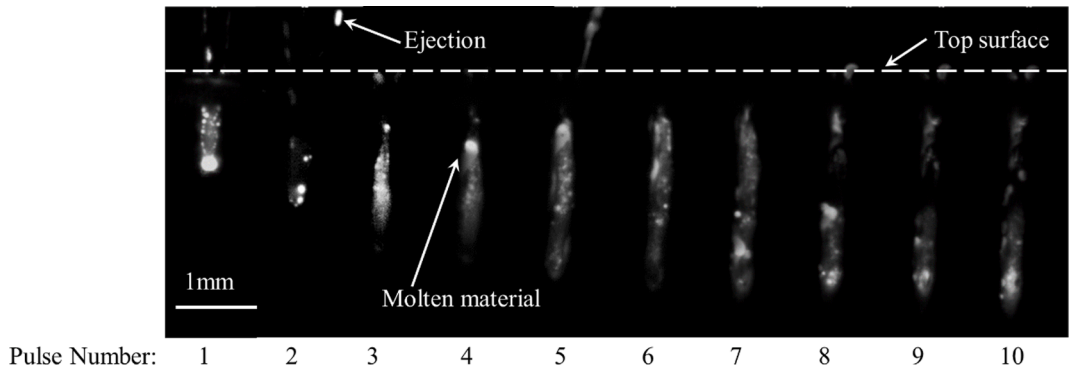

Fig. 3. Keyhole evolution under different pulse number during multi-pulse drilling process.

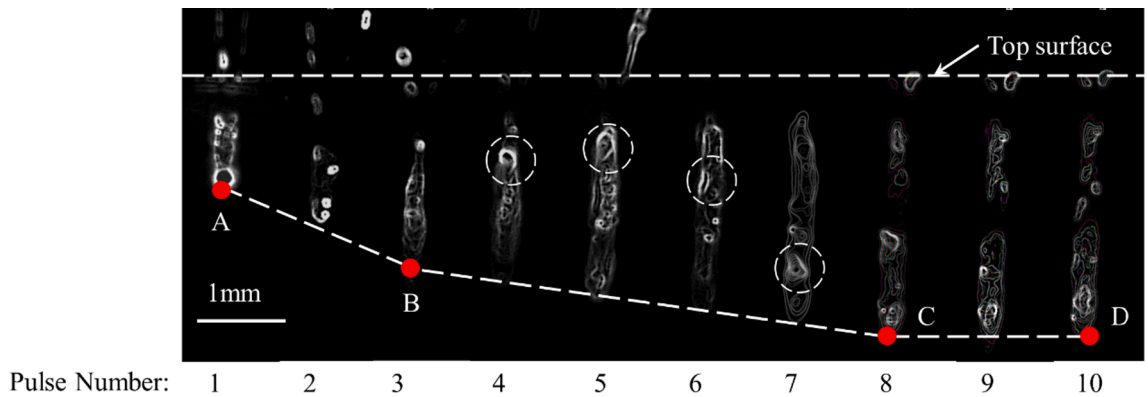

Fig. 4. Keyhole profile and molten material in each pulse cycle after edge detection.

drilling period, the depth of keyhole barely changed as the number of laser pulse increased. There was no melt ejection near the entrance. Many droplets of molten material were dispersed at keyhole wall, and the keyhole was wavy.

As seen in Fig. 4, the keyhole profile and the molten pool behavior were different in three periods. It was mainly because that the energy exchange at vapor/liquid interface was different at different period. Due to the Gaussian distribution of laser beam, the laser power density was high (about 1.41 ~ 2.56 MW/cm^2) when the keyhole was shallow during rapid drilling period. On the contrary, the laser power density was low (about 0.46 MW/cm^2) when the keyhole was deep during moderate drilling period. As a result, the energy exchange at vapor/liquid interface was different at different period. The temperature distribution at vapor/liquid interface and driving forces were also different at different period. In this TVS, the competition mechanism between driving forces determined the dynamic behavior of melt flow. However, the melt flow behavior and the effect of driving forces on that could not be observed through the use of in-situ observation system. Hence, in order to investigate the melt flow transition and its influence factors, the flow dynamic behavior was investigated by using the developed numerical model.

4.2. Dynamic behavior of melt flow during rapid drilling period

As shown in Fig. 5, the keyhole evolution during the first pulse cycle of rapid drilling period was simulated by considering three driving forces: gravity, surface tension and recoil pressure. When the laser was on, the laser power density was high and the high temperature zone was located in keyhole bottom. As a result, the keyhole depth increased rapidly and the keyhole shape was conical. From 0.40 ms, the molten material near the entrance moved up and then was ejected. When the laser was off, the temperature dropped and the temperature of molten material near keyhole entrance was the highest. At 0.75 ms, the unejected material flowed back and a hump occurred near the keyhole entrance in the end.

When the laser was on, as shown in Fig. 6(a), the melt flow moved upwards and the thin liquid layer was wide at the top and narrow at the bottom. In order to figure out the effects of driving forces on melt flow behavior, the numerical simulations without considering gravity (g), surface tension (σ) and recoil pressure (P_{re}), were performed, respectively. There was the strategy of neglecting driving force: 1) When the effect of driving forces within the pulse width is investigated, the driving force is neglected from initial moment (0.0 ms) to the end of pulse width (0.6 ms). 2) When the effect of driving forces within the interpulse time is investigated, the driving force is neglected from the end of pulse width (0.6 ms) to the end of pulse period (10.0 ms).

When the laser was on, the final keyhole (0.6 mm) without considering gravity was simulated as shown in first image of Fig. 6(b). Compared with the result considering all forces, the liquid layer was thinner, and the velocity direction of the molten material was still upward. This maybe because that more molten material was ejected without being driven by gravity and fewer of that remained inside keyhole. Hence, it can be inferred that the gravity was the reason for causing a wide top and narrow bottom liquid layer. Due to the thin liquid layer near the hole entrance, the molten material solidified quickly and there was no backflow. Hence, the unejected material due to gravity near the hole entrance was the precondition for the occurrence of the backflow in this period. Without considering surface tension, the final keyhole was simulated as shown in second image of Fig. 6(b). Without considering the effect of surface tension, there was a backflow at the hole entrance. Therefore, the surface tension was a contributory cause of the upward movement for melt near the hole entrance. Without considering recoil pressure, the final keyhole was simulated as shown in last image of Fig. 6(b). It can be seen that there was no keyhole. Hence,

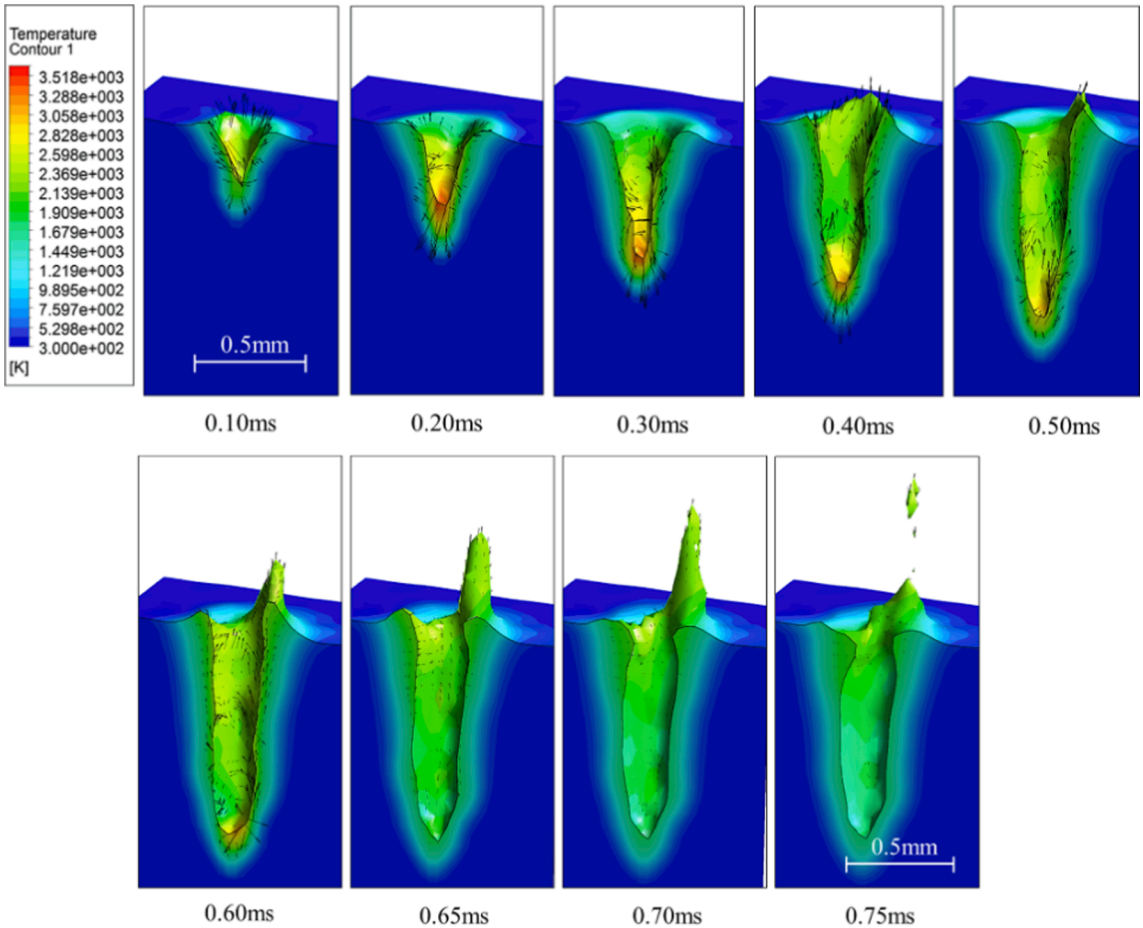

Fig. 5. Keyhole evolution during the first pulse cycle of rapid drilling period.

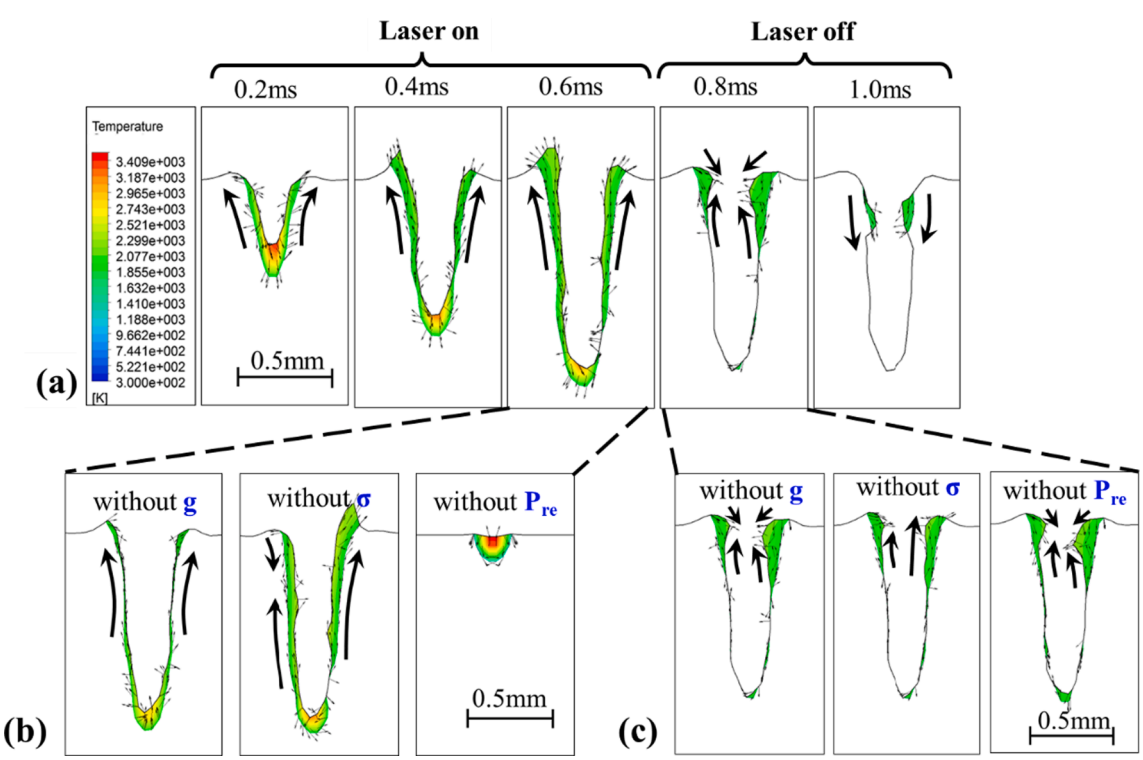

Fig. 6. (a) Melt flow behavior, (b) effect of driving forces when the laser was on and (c) effect of driving forces when the laser was off during first pulse cycle of rapid drilling period.

at this stage, the impact of recoil pressure was dominant. Driven by recoil pressure, the melt flowed upwards and the molten material was ejected, which led to a rapidly increased keyhole depth and a conical keyhole.

When the laser was off, the melt cooled down quickly. At 0.8 ms, the molten material near the keyhole bottom solidified firstly, and that near the entrance remained molten. There was a downward melt flow at the top of the molten pool due to the melt back-flow. The converging of the opposite flow decreased the velocity of the upward melt flow and led to a hump beneath the keyhole entrance.

Through the use of numerical simulation, the reason of back flow was figured out. As shown in Fig. 6(c), without considering the effects of gravity and recoil pressure, the melt flow behavior was similar with that when considering all driving forces. However, when the effect of surface tension was neglected, the backflow at the hole entrance disappeared. Hence, it can be seen that the back flow of melt in this stage was caused by surface tension. The effects of gravity and recoil pressure could be neglected.

4.3. Dynamic behavior of melt flow during linear drilling period

As shown in Fig. 7, the keyhole evolution during the first pulse cycle of linear drilling period was simulated by considering three driving forces. Due to the solidification of the backflow material at previous cycles, there was a hump near the keyhole entrance as indicated with white dotted circles. The hump and the keyhole bottom were heated when irradiated by the laser pulse. Hence, there were two molten zones inside keyhole within first 0.5 ms, as indicated with red circles. With time going on, the two molten zones gradually became one and the amount of the molten material gradually increased. As a result, when the laser was off, the molten material flowed back, which led to a keyhole blockage.

When the laser was on, the melt flow moved upwards at the beginning of the laser drilling, as indicated in Fig. 8(a). At 0.4 ms, the hump near the entrance melted and expanded both upwards and downwards. There was a backflow inside the molten pool at keyhole bottom, which led to a collision of the melt flow. At 0.6 ms, those two molten zones merged into one and the collision of convection continued.

The numerical results, as indicated in Fig. 8(b), showed that when the effect of gravity was neglected, there was no downward melt flow inside molten pool. Thus, the gravity was responsible for the melt flowing downwards. When the effect of surface tension was neglected, there were downward flow at the middle of molten pool and upward flow at the top and bottom of that. When the effect of recoil pressure was neglected, the keyhole was shallower and the temperature of the molten material was higher than the others. Hence, the recoil pressure was responsible for the melt flowing upwards. To summarize, when the laser was on during the linear drilling period, the upward melt flow was caused by recoil pressure and the downward melt flow was caused by surface tension and gravity. Compared with the first and second image in Fig. 8(b), it can be deduced that the effect of gravity was greater than that of surface tension.

When the laser was off, the collision of the melt flow caused a keyhole blockage. Inside the blockage region, there were two vortices.

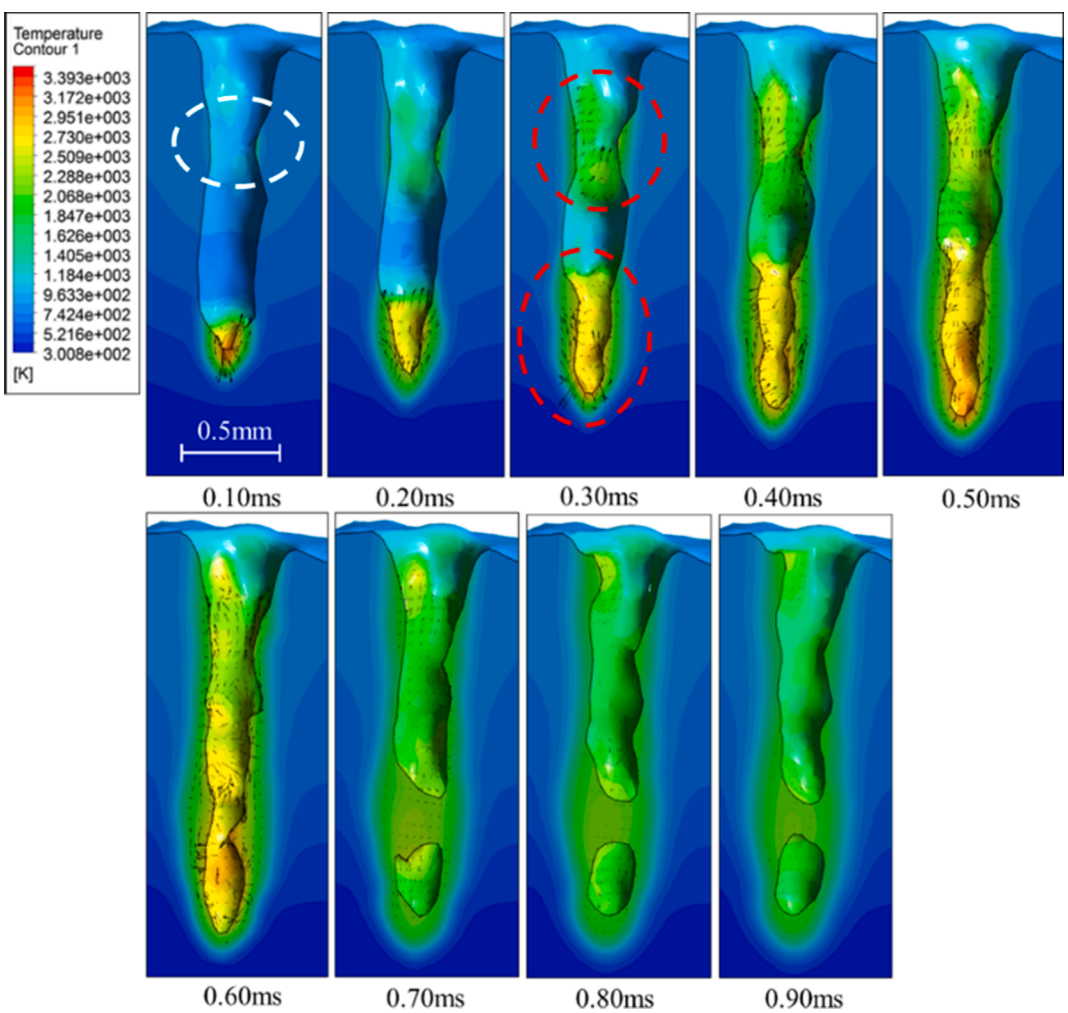

Fig. 7. Keyhole evolution during the first pulse cycle of linear drilling period.

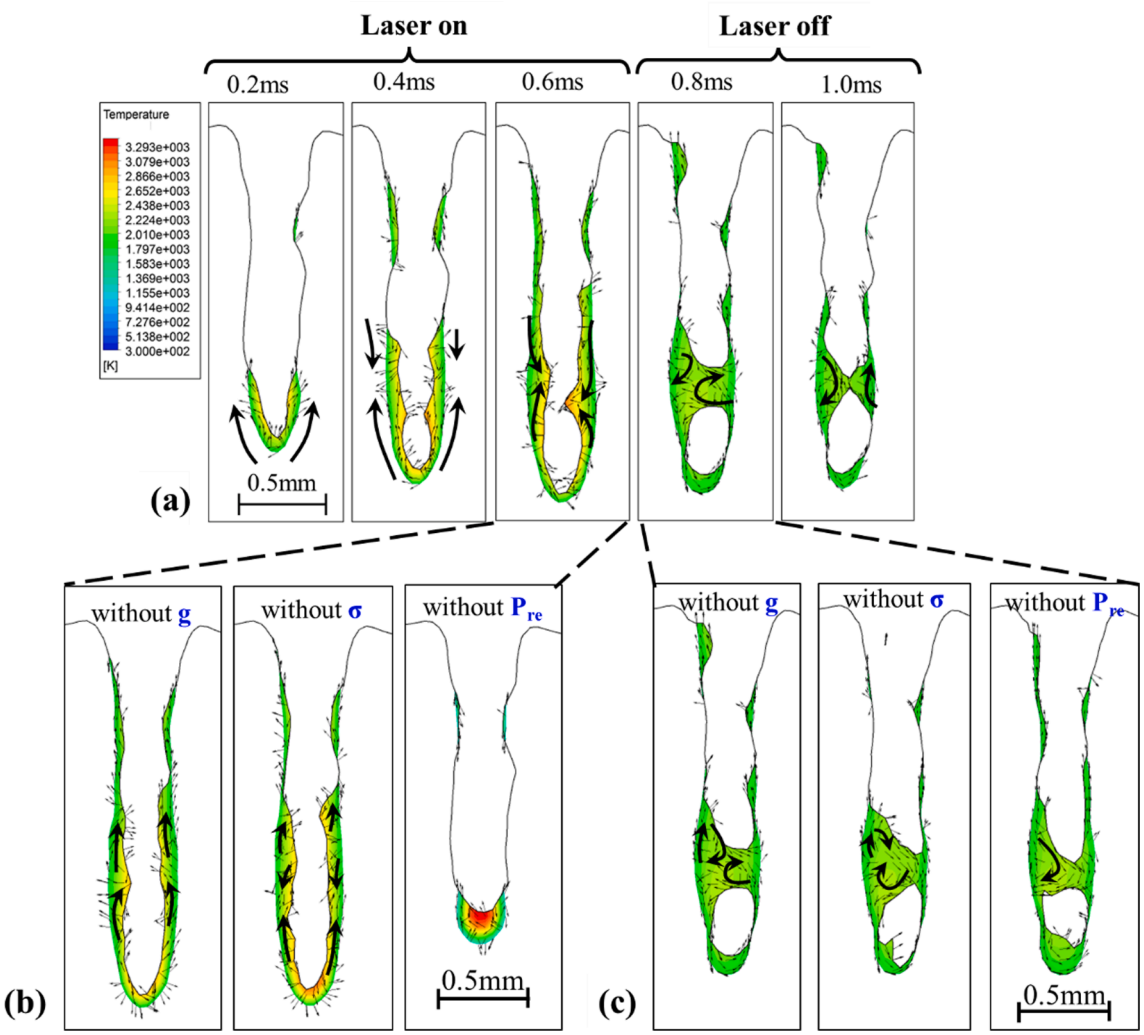

Fig. 8. (a) Melt flow behavior, (b) effect of driving forces when the laser was on and (c) effect of driving forces when the laser was off during first pulse cycle of linear drilling period.

The upper left vortex flow came from the melt backflow, and the lower right vortex flow came from the upward movement of the molten material.

From Fig. 8(c), it can be seen that without considering the effect of gravity, the keyhole profile and melt flow behavior hardly changed compared with those considering all driving forces. Without considering the effect of surface tension, the volume of upper left blockage region was larger and the change of melt flow direction was slower than that with considering the effects of all driving forces. Hence, the surface tension could boost the motion of vortex. Without considering the effect of recoil pressure, the lower right vortex flow disappeared and some molten material remained at the keyhole bottom. The volume of the blockage region was smaller than the others. In conclusion, when the laser was off during the linear drilling period, the upper left vortex flow was driven by the surface tension dominantly, and the lower right vortex flow was driven by the recoil pressure. The collision of the melt flow and the keyhole blockage resulted from surface tension and recoil pressure.

4.4. Dynamic behavior of melt flow during moderate drilling period

The keyhole evolution during the first pulse cycle of moderate drilling period was simulated as shown in Fig. 9. At the initial time of the laser irradiation, the temperature for the keyhole wall increased a little and there was hardly any molten material inside the keyhole. At 0.2 ms, a large molten pool appeared at the bottom of keyhole, and some small molten zones dispersed at keyhole walls. With time going on, the molten zones at the bottom of keyhole merged into one. Due to deep keyhole and defocusing effect of laser beam, the laser power density was low and the increment of depth was small. When the laser was off, the molten material cooled down and the keyhole profile was wavy.

The melt flow behavior during the first pulse cycle of moderate drilling period was indicated in Fig. 10(a). At 0.2 ms, there were three molten zones inside keyhole, as marked in the first image of Fig. 10(a). Molten pool A was the biggest one among the three zones and spread upwards. At 0.4 ms, these three molten zones became one (marked as A'). Inside of molten pool A', there was collision of the melt flow at the positions indicated by the blue arrows, which was induced by the mergence of molten zones. At 0.6 ms, the collision resulted in two protuberances at the positions indicated by the black arrows. Besides, at 0.4 ms, there were two small molten zones B' and C' over the molten pool A'. The behavior of these three molten zones was similar with the molten zones A, B and C. The collision and the protuberances caused by these three molten zones were indicated by the blue dotted arrows and black dotted arrows in Fig. 10(a). As a result, the mergence of those dispersed molten zones resulted in a wavy keyhole. When the laser was off, the molten material cooled down and solidified, and the keyhole profile remained wavy.

Fig. 10(b) showed the effects of driving forces on melt flow when the laser was on during first pulse cycle of moderate drilling period. When the effect of gravity was ignored, the position for the melt flow collision

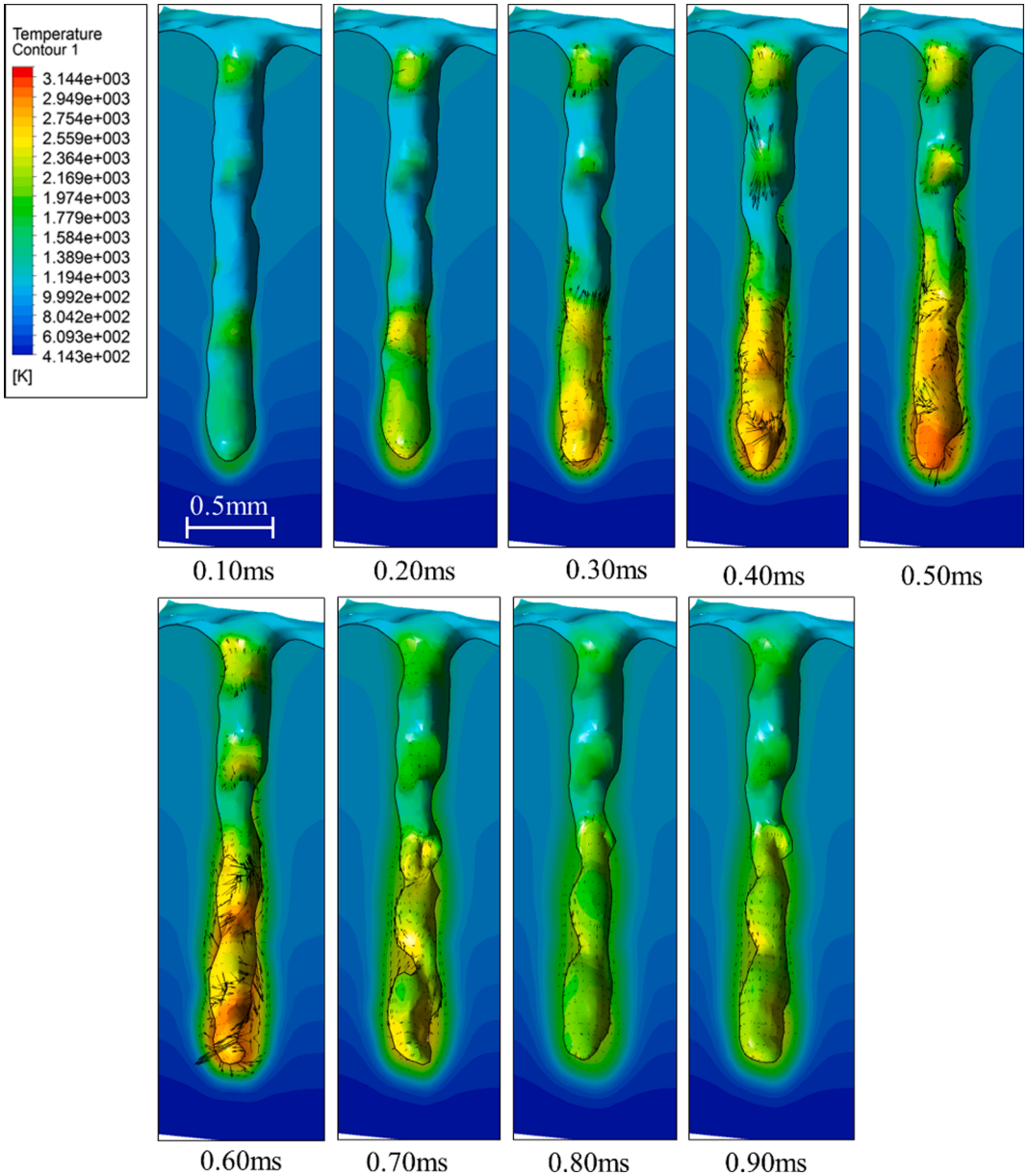

Fig. 9. Keyhole evolution during the first pulse cycle of moderate drilling period.

moved up. When the effect of surface tension was ignored, the position for the melt flow collision moved up and it was higher than the others. When the effect of recoil pressure was ignored, there were some molten material at the keyhole bottom, and the keyhole was a little shallower than the others. In conclusion, when the laser was on during the moderate drilling period, the impact of surface tension was dominate compared with the impact of gravity on the downward flow, and the recoil pressure was responsible for the melt flow upwards.

The effects of driving forces on melt flow when the laser was off during first pulse cycle of moderate drilling period were indicated in Fig. 10(c). When the effect of surface tension was ignored, some molten material inside keyhole was ejected and molten material at the keyhole bottom was pushed up. When the effect of recoil pressure was ignored, some molten material flowed downwards. In conclusion, when the laser was off during the moderate drilling period, it could be seen that the effects of surface tension and recoil pressure were dominate.

As discussed above, the keyhole evolution process druing multi-pulse drilling could be divided into three periods. Morphology characteristics, melt flow behavior and main driving forces during these three stages were summeried in Table 2. It can be seen that the flow transition and its influence factors were figured out, which was beneficial to the understanding of the evolution process of molten pool during multi-pulse drilling with millisecond laser. The dynamic change of driving forces was responsible for the transition of melt flow pattern and determined the quality of drilled hole. During the linear drilling and moderate drilling period, some defects such as blockage and low repeatability (unpredictable wave motion of keyhole) resulted from a lack of expulsion force. In other words, the recoil pressure was not enough. In oreder to overcome this problem, sevaral methods could be used. Firstly, the laser power density could be increased for enhancing the recoil pressure by moving the focal plane at linear drilling and moderate drilling period. Also, the auxiliary gas could be used at a appropriate pressure to expel the molten material out together with recoil pressure.

As shown in Fig. 11, the keyhole depth and keyhole profile from high-speed photography agree well with those from simulation. In Fig. 11(b) and (c), the occurrence of the melt hump as indicated with red circles was predicted, but the positions of those predicted from in-situ observation and simulation were different. This maybe because of

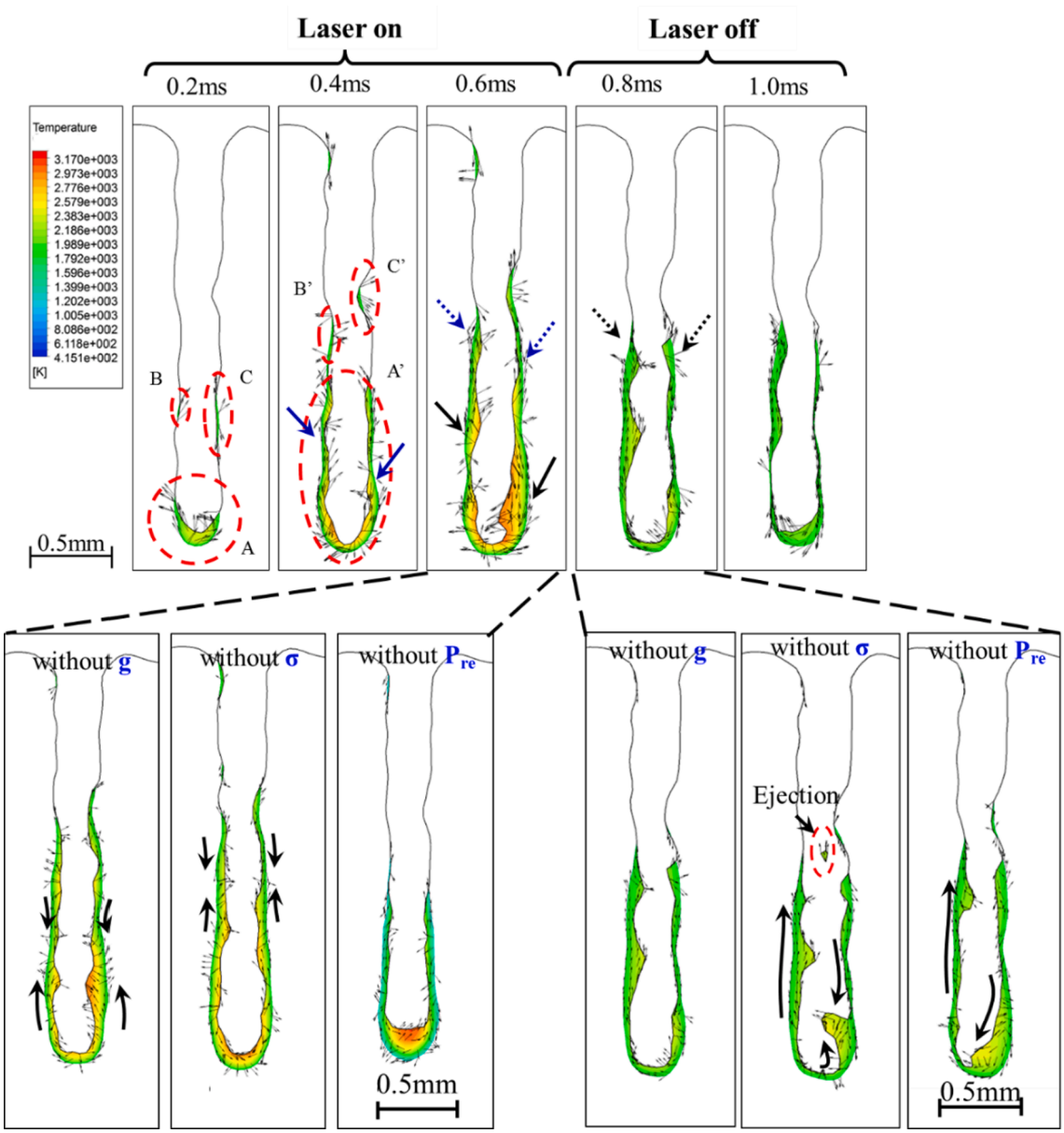

Fig. 10. (a) Melt flow behavior, (b) effect of driving forces when the laser was on and (c) effect of driving forces when the laser was off during first pulse cycle of moderate drilling period.

lacking considering the effect of auxiliary gas flow in numerical model, which could be optimized later. Furthermore, the fluid dynamics was also affected by the process parameters, such as defocus amount, pulse duration, duty cycle and so on. For example, if the difference of defocus amount was large, the keyhole shape was totally different and the melt flow behavior was totally different. When the defocus amount was positive, the keyhole was conical and the diameter of hole entrance was large. Hence, it was easier for the melt ejection than that when drilling at focal plane. In this situation, the keyhole blockage rarely occurred. The influence of process parameters on fluid dynamics of melt pool will be further investigated in the future.

5. Conclusions

In this paper, by combining in-situ observation and numerical simulation methods, the whole process of dynamic evolution of keyhole, the transition of flow pattern and the impacts of driving forces on the transition during multi-pulse drilling process are systematically investigated. Following conclusions can be made:

1. During the multi-pulse drilling process, the material removal rate, keyhole profile, melt flow behavior, and driving forces change with the increase of pulse number. Through the use of in-situ observation method, the multi-pulse drilling process can be divided into three periods according to the material removal rate: rapid drilling period, linear drilling period, and moderate drilling period.
2. In rapid drilling period, the keyhole is conical with hump. When the laser is on, the molten material moves upward, driven by recoil pressure and some molten material accumulates at the entrance. When the laser is off, the molten material flows back under the driving of surface tension, then it solidifies, which leads to a hump near the entrance.
3. In linear drilling period, there is a blockage inside keyhole. When the laser is on, the gravity drives the melt flow downwards and the recoil pressure pushes the melt flow upwards. The collision of the opposite flow inside a molten pool leads to humps. When the laser is off, the

Table 2
Morphology characteristics, melt flow behavior and main driving forces during keyhole evolution process during multi-pulse drilling.

Keyhole evolution process	Morphology characteristics	Laser on (0.6 ms)		Laser off (0.8 ms)	
		Melt flow	Driving forces	Melt flow	Driving forces
Rapid drilling	Conical with hump	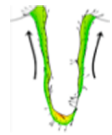	Recoil pressure		Surface tension
Linear drilling	Blockage	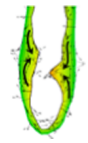	Gravity Recoil Pressure		Surface tension Recoil Pressure
Moderate drilling	Wavy	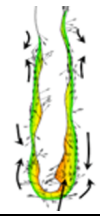	Surface tension Recoil Pressure		Surface tension Recoil Pressure

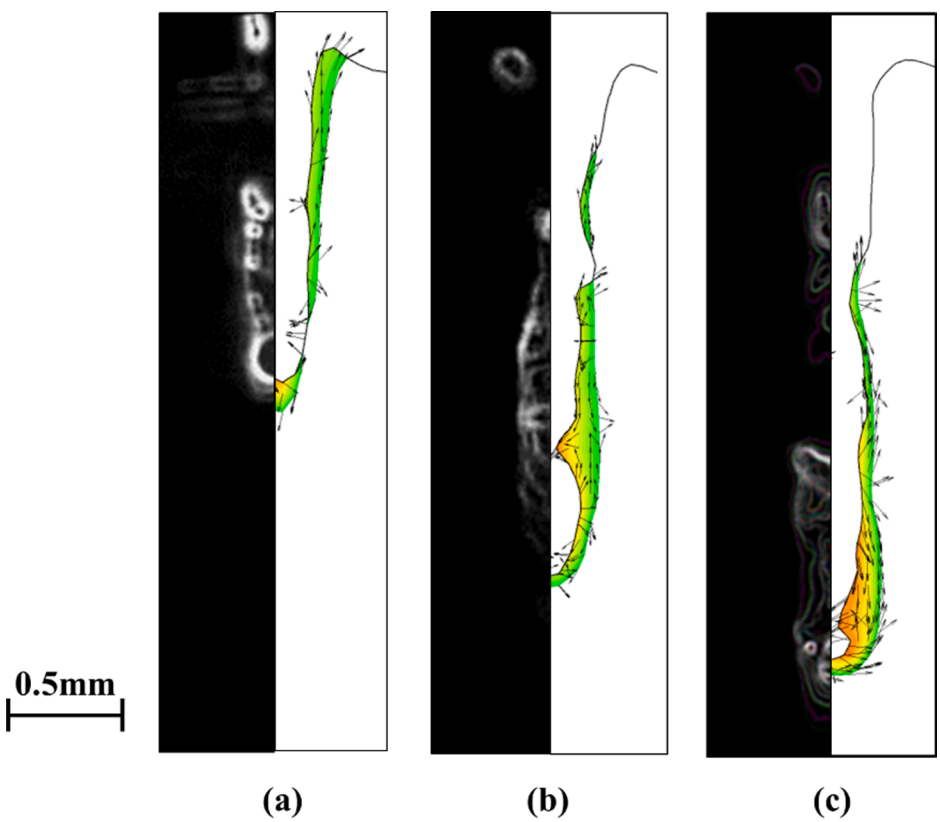

Fig. 11. Comparison between keyhole profile from high-speed photography and simulated keyhole profile (a) first pulse of rapid drilling period; (b) first pulse of linear drilling period; (c) first pulse of moderate drilling period.

humps result in a blockage driven by surface tension and recoil pressure.

4. In moderate drilling period, the keyhole is wavy. During the whole period, the molten material is driven by surface tension and recoil pressure dominantly. In this period, some small molten zones disperse at keyhole walls. With the development of those molten zones, they merge into one. In the process of mergence, collision of the opposite flow leads to humps, which solidify and bring about a wavy keyhole.

CRediT authorship contribution statement

Yue Zhang: Investigation, Conceptualization, Methodology, Writing – original draft, Writing – review & editing. **Xiuli He:** Supervision,

Writing – review & editing, Conceptualization. **Gang Yu:** Supervision, Writing – review & editing, Conceptualization. **Shaoxia Li:** Supervision, Writing – review & editing. **Chongxi Tian:** Writing – review & editing. **Weijian Ning:** . **Yanmei Zhang:** .

Declaration of Competing Interest

The authors declare that they have no known competing financial interests or personal relationships that could have appeared to influence the work reported in this paper.

References

[1] W. Perrie, A. Rushton, M. Gill, P. Fox, W. O'Neill, Femtosecond laser micro-structuring of alumina ceramic, Appl. Surf. Sci. 248 (1-4) (2005) 213–217.

[2] K.T. Voisey, S.S. Kudesia, W.S.O. Rodden, D.P. Hand, J.D.C. Jones, T.W. Clyne, Melt ejection during laser drilling of metals, Mat. Sci. Eng. A-Struct.: A 356 (1-2) (2003) 414–424.

[3] T. Kampe, S. Völker, F. Zehe, A Model for Cylindrical Hole Film Cooling: Part I-A Correlation for Jet-Flow With Application to Film Cooling, J. Turbomach. 134 (2012), 061010.

[4] Y. Liu, J. Wang, W. Li, C. Wang, Q. Zhang, X. Yang, L. Cheng, Effect of energy density and feeding speed on micro-holes drilling in SiC/SiC composites by picosecond laser, Int. J. Adv. Manuf. Technol. 84 (9-12) (2016) 1917–1925.

[5] Z. Zhai, W. Wang, X. Mei, Simulation and experimental study on laser drilling of nickel-based alloy with thermal barrier coatings, Int. J. Adv. Manuf. Technol. 90 (5-8) (2017) 1871–1879.

[6] M. Chen, Y. Wang, G. Yu, D. Lan, Z. Zheng, In situ optical observations of keyhole dynamics during laser drilling, Appl. Phys. Lett. 103 (19) (2013) 194102, https://doi.org/10.1063/1.4829147.

[7] W. Duan, X. Dong, K. Wang, Z. Fan, X. Mei, W. Wang, J. Lv, Effect of temporally modulated pulse on reducing recast layer in laser drilling, Int. J. Adv. Manuf. Technol. 87 (5-8) (2016) 1641–1652.

[8] H. Ki, P.S. Mohanty, J. Mazumder, Modelling of high-density laser–material interaction using fast level set method, J. Phys. D Appl. Phys. 34 (3) (2001) 364–372.

[9] C.-C. Ho, Y.-J. Chang, J.-C. Hsu, C.-M. Chiu, C.-L. Kuo, Optical emission monitoring for defocusing laser percussion drilling, Measurement 80 (2016) 251–258.

[10] I. Arrizubieta, A. Lamikiz, S. Martínez, E. Ukar, I. Tabernero, F. Girot, Internal characterization and hole formation mechanism in the laser percussion drilling process, Int. J. Mach. Tool Manu. 75 (2013) 55–62.

[11] S.H. Alavi, S.P. Harimkar, Evolution of geometric and quality features during ultrasonic vibration-assisted continuous wave laser surface drilling, J. Mater. Process. Technol. 232 (2016) 52–62.

[12] S. Sharma, V. Mandal, S.A. Ramakrishna, J. Ramkumar, Numerical simulation of melt hydrodynamics induced hole blockage in Quasi-CW fiber laser micro-drilling of TiAl6V4, J. Mater. Process. Technol. 262 (2018) 131–148.

[13] K. Walther, M. Brajdic, E.W. Kreutz, Enhanced processing speed in laser drilling of stainless steel by spatially and temporally superposed pulsed Nd:YAG laser radiation, Int. J. Adv. Manuf. Technol. 35 (9-10) (2008) 895–899.

[14] S. Asai, I. Muchi, Theoretical analysis and model experiments on the formation mechanism of channel-type segregation, Trans. Iron Steel Inst. Jpn. 18 (2) (1978) 90–98.

[15] C.J. Knight, Theoretical modeling of rapid surface vaporization with back pressure, AIAA J. 17 (5) (1979) 519–523.

[16] S.I. Anisimov, V.A. Khokhlov, Instabilities in laser-matter interaction, CRC Press (1995).

[17] A.F.H. Kaplan, Absorption homogenization at wavy melt films by CO2-lasers in contrast to 1 μm-wavelength lasers, Appl. Surf. Sci. 328 (2015) 229–234.

[18] W.-I. Cho, S.-J. Na, C. Thomy, F. Vollertsen, Numerical simulation of molten pool dynamics in high power disk laser welding, J. Mater. Process. Technol. 212 (1) (2012) 262–275.

[19] V. Semak, A. Matsunawa, The role of recoil pressure in energy balance during laser materials processing, J. Phys. D Appl. Phys. 30 (18) (1997) 2541–2552.

[20] Y. Zhang, G. Yu, X.L. He, S.X. Li, W.J. Ning, Driving mechanism of keyhole evolution during multi-pulse drilling with a millisecond laser, Sci. China-Phys. Mech. Astron 62 (10) (2019), https://doi.org/10.1007/s11433-019-9418-4.

[21] J. Canny, A computational approach to edge detection, IEEE T Pattern Anal. PAMI-8 (6) (1986) 679–698.